



CHORUS

This is the accepted manuscript made available via CHORUS. The article has been published as:

Magnetic properties of the triangular lattice magnets
 $A_4B^{\prime}B_2O_{12}$ ($A = \text{Ba, Sr, La}$; $B^{\prime} = \text{Co, Ni, Mn}$;
 $B = \text{W, Re}$)

R. Rawl, M. Lee, E. S. Choi, G. Li, K. W. Chen, R. Baumbach, C. R. dela Cruz, J. Ma, and H.
D. Zhou

Phys. Rev. B **95**, 174438 — Published 25 May 2017

DOI: [10.1103/PhysRevB.95.174438](https://doi.org/10.1103/PhysRevB.95.174438)

Magnetic Properties of New Triangular Lattice Magnets $A_4B'B_2O_{12}$

R. Rawl,¹ M. Lee,^{2,3} E. S. Choi,³ G. Li,⁴ K. W. Chen,³ R. Baumbach,³ C. R. dela Cruz,⁵ J. Ma,^{6,1} and H. D. Zhou^{1,3}

¹Department of Physics and Astronomy, University of Tennessee, Knoxville, Tennessee 37996-1200, USA

²Department of Physics, Florida State University, Tallahassee, Florida 32306-3016, USA

³National High Magnetic Field Laboratory, Florida State University, Tallahassee, Florida 32310-3706, USA

⁴School of Physics and Materials Science, Anhui University, Hefei, Anhui, 230601, People's Republic of China

⁵Quantum Condensed Matter Division, Oak Ridge National Laboratory, Oak Ridge, Tennessee 37831, USA

⁶Department of Physics and Astronomy, Shanghai Jiao Tong University, Shanghai 200240, People's Republic of China

The geometrically frustrated two dimensional triangular lattice magnets $A_4B'B_2O_{12}$ ($A = \text{Ba, Sr, La}$; $B' = \text{Co, Ni, Mn}$; $B = \text{W, Re}$) have been studied by x-ray diffraction, AC and DC susceptibilities, and powder neutron diffraction, and specific heat measurements. The results reveal that (i) the samples containing Co^{2+} (effective spin-1/2) and Ni^{2+} (spin-1) ions with small spin numbers exhibit ferromagnetic (FM) behavior and ordering, respectively, while the sample containing Mn^{2+} (spin-5/2) ions with a large spin number exhibits antiferromagnetic (AFM) ordering. We ascribe these spin number manipulated ground states to the competition between the AFM $B'-O-O-B'$ and FM $B'-O-B-O-B'$ superexchange interactions; (ii) the chemical pressure introduced into the Co containing samples through the replacement of different size ions on the A site finely tunes the FM behavior temperature of the system. This effect is not simply governed by the lattice parameters, and requires more precise structural measurements to elucidate.

PACS numbers: 75.47.Lx, 75.30.Et, 61.05.F-

I. INTRODUCTION

Geometrically frustrated magnets have attracted much attention for the novel properties they exhibit at low temperatures such as spin ice, spin liquids, non-collinear ground states, and fractional gauge fields¹⁻³. Of particular interest are the two dimensional (2D) triangular lattice magnets (TLMs) as, despite their simple structure, they can be host to a multitude of ground states⁴⁻⁶. There are several examples: (i) $\text{Ba}_3\text{CoSb}_2\text{O}_9$ ⁷⁻¹⁰, with equilateral Co^{2+} (effective spin-1/2) triangular lattice, exhibits a 120 degree ordered state at zero field and an up up down phase with applied field. Although its spin wave spectrum can be reasonably described by the

XXZ model with a small easy plane anisotropy, the quantum spin fluctuations still lead to abnormal magnon decay and line broadening that cannot be accounted for by linear and nonlinear spin wave theories¹¹; (ii) $\text{Ba}_3\text{BNb}_2\text{O}_9$ ($B = \text{Co}^{12,13}$, Ni^{14} , Mn^{15}), CuCrO_2 ^{16,17}, and $\text{RbFe}(\text{MoO}_4)_2$ ^{18,19} exhibit interesting multiferroic properties in the 120 degree ordered state; (iii) 2H-AgNiO_2 ^{20,21} is a rare TLM that shows ordering with a collinear alternating stripe pattern which could be related to its strong easy axis anisotropy; (iv) $\text{A}\text{Ag}_2\text{M}(\text{VO}_4)_2$ ($A = \text{Ba, Sr}$; $M = \text{Co, Ni}$)^{22,23} are TLMs possessing ferromagnetic (FM) orderings due to superexchange via the bridging vanadates on a triangular lattice; (v) NaVO_2 ^{24,25} is a rare TLM exhibiting ordering of the V^{3+} orbitals. Consequently, this orbital ordering relieves the geometrical frustration and leads to long range magnetic ordering; (vi) shown recently, the exotic quantum spin liquid (QSL) state is realized in YbMgGaO_4 ²⁶⁻²⁹ with an effective spin-1/2 Yb^{3+} triangular lattice in which the spin anisotropy and next-nearest neighbor interactions play important roles.

To investigate all of these intriguing ground states, the discovery and exploration of new examples of TLMs is necessary. From a materials engineering perspective, one possible way to realize the 2D triangular lattice is by a stacked layer model, for example in the perovskite structure^{30,31}. The basic perovskite structure (ABO_3) can be considered as consisting of 3 layers of AO_3 with layers of B ions in between. The A and B site ions form corner sharing octahedra with the surrounding oxygens. Alternately, adjacent layers may consist of edge sharing oxygen octahedra, opening up further stacking mechanisms to be explored in a plethora of compounds³⁰. Of interest in realizing true 2D behavior is the presence of vacant layers where neither a magnetic nor non-magnetic ion resides. This vacancy helps to ensure that interlayer interactions are small compared to intralayer interactions.

Based on this principle, we examine new 2D TLMs utilizing close-packed stacking of perovskite layers. A promising

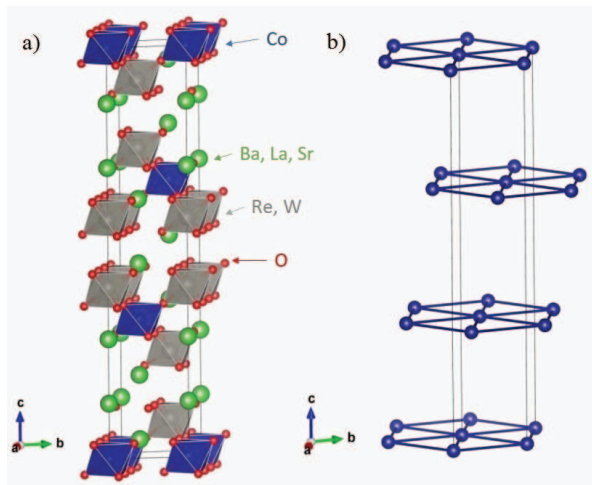


FIG. 1: (color online) a) Crystalline structure of $A_4\text{CoB}_2\text{O}_{12}$ with the space group $R\bar{3}mH$. b) Staggered pattern of triangular Co^{2+} planes along the c -axis

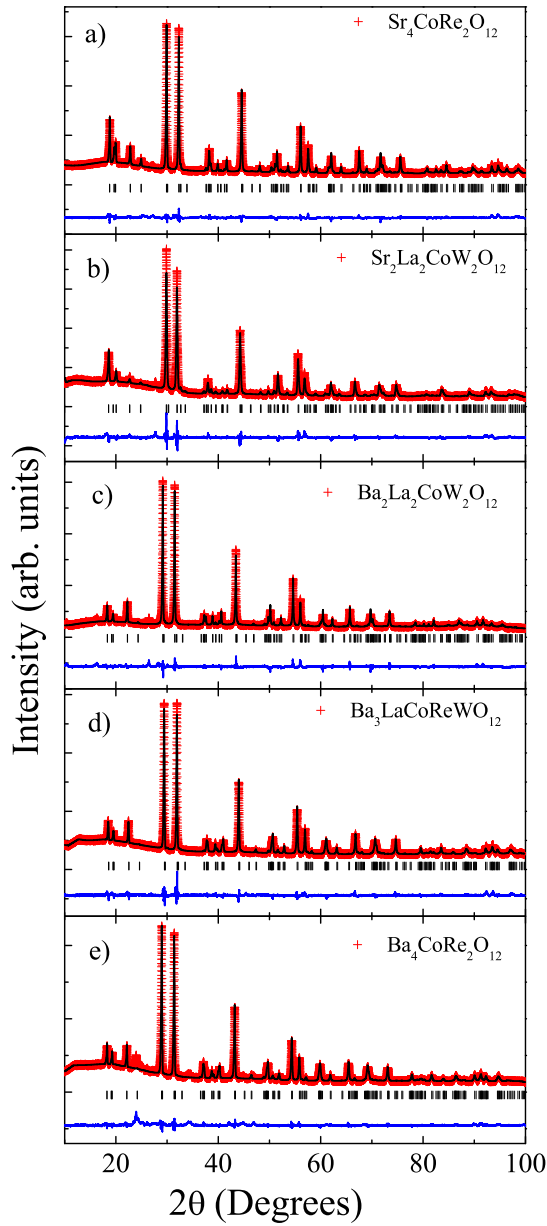


FIG. 2: (color online) a-e) Powder x-ray diffraction patterns (red cross) and Rietveld refinements (black line) for five $A_4CoB_2O_{12}$ compounds. The blue lines at the bottom of each panel is the difference curve. The black ticks are the reflection positions.

structure is $A_4B'B_2O_{12}$ ($A = Ba, Sr, La$; $B' = Co, Ni, Mn$; $B = W, Re$). In this structure, using $A_4CoB_2O_{12}$ as the example shown in Fig. 1, the magnetic Co^{2+} ions and nonmagnetic W^{6+}/Re^{7+} ions occupy the octahedral sites in the perovskite layers in an ordered fashion at the $(3a)$ and $(6c)$ positions, respectively. Thus, the CoO_6 octahedral layer forms a Co^{2+} -triangular lattice in the ab plane. Here the Co octahedra are corner sharing with the adjacent W/Re octahedra and this Co layer is sandwiched by two (W/Re) O_6 layers. Moreover, the octahedral interstices between the two adjacent W/Re layers

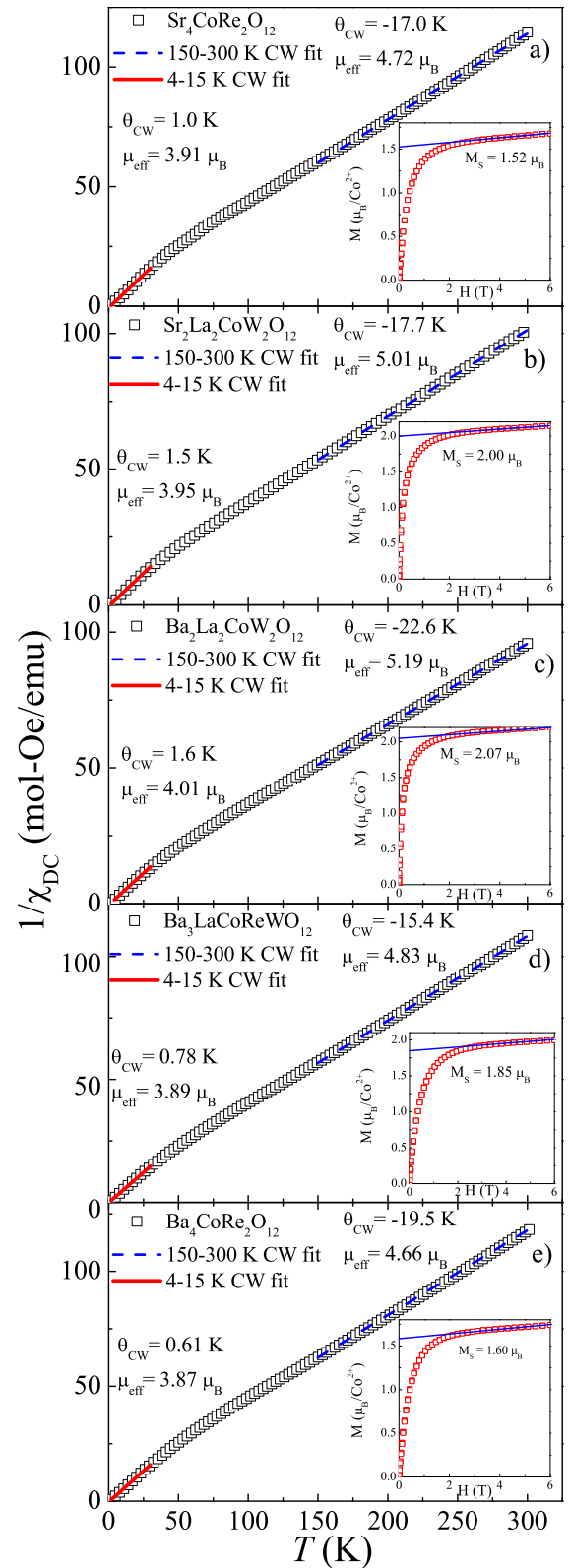


FIG. 3: (color online) a-e) The inverse DC susceptibility for the $A_4CoB_2O_{12}$ compounds. The solid and dashed lines are Curie-Weiss fittings of the low temperature and high temperature regimes, respectively. Inserts: DC magnetization taken at 1.8 K. The saturation magnetization of the Co^{2+} ion is extrapolated by using a linear fit to account for the Van Vleck paramagnetic contribution.

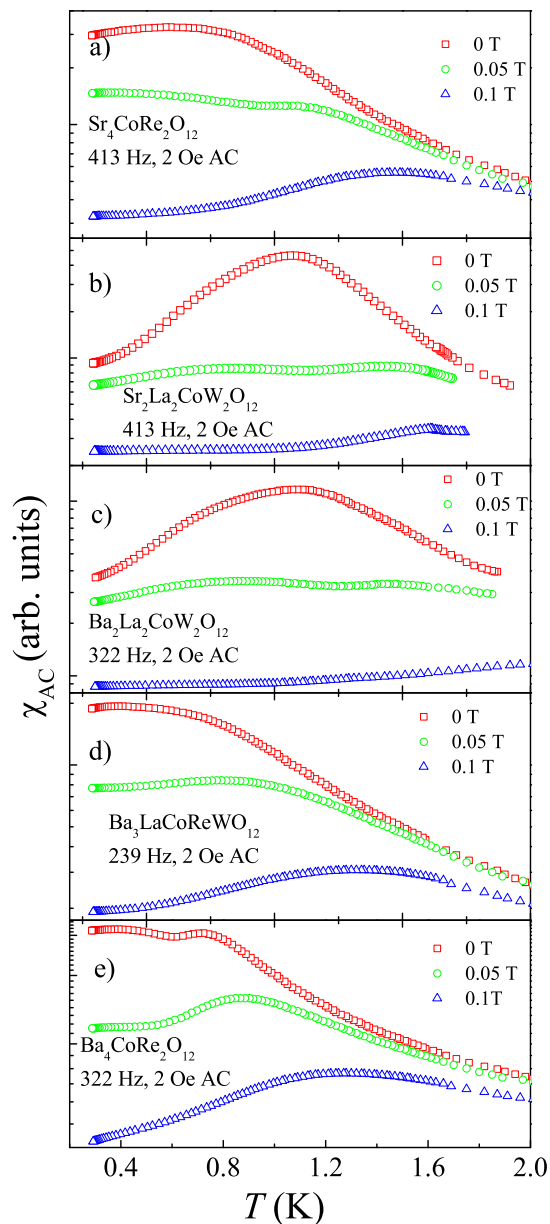


FIG. 4: (color online) a-e) The real part of the AC susceptibility (χ_{AC}) for cobalt containing $A_4B'B_2O_{12}$ compounds measured from 0.3 to 2.0 K under different DC magnetic fields. Excitation fields of 2 Oe at low AC frequencies were used.

are vacant to accommodate the strong electric repulsion of the W^{6+}/Re^{7+} ions. The separation of the layers of Co^{2+} by two layers of W^{6+}/Re^{7+} and one vacant layer significantly reduces the interplane interactions and enhances the 2D nature of this structure. More intriguingly, due to the flexible chemistry in this structure, we can easily (i) introduce chemical pressure into the system by changing the lattice parameters. For example, within the set of samples, $Sr_4CoRe_2O_{12}$, $Sr_2La_2CoW_2O_{12}$, $Ba_2La_2CoW_2O_{12}$, $Ba_3LaCoReWO_{12}$, and $Ba_4CoRe_2O_{12}$, we expect the lattice parameters will change

accordingly as we replace Sr^{2+} ions with larger La^{2+} and even larger Ba^{2+} ions; (ii) change the spin numbers of the system by varying magnetic the B' ions. For example, within the set of samples $Ba_2La_2CoW_2O_{12}$, $Ba_2La_2NiW_2O_{12}$ and $Ba_2La_2MnW_2O_{12}$, the spin numbers change from effective spin-1/2 (Co^{2+}) to spin-1 (Ni^{2+}), and spin-5/2 (Mn^{2+}). Therefore, the $A_4B'B_2O_{12}$ structure provides an ideal platform to study the magnetic properties of new TLMs and how the perturbations, such as chemical pressure and spin numbers, affect them. So far, while the structures of several $A_4B'B_2O_{12}$ members have been reported³²⁻³⁴ and the susceptibility of $Ba_2La_2MnW_2O_{12}$ ³⁵ has been measured down to 2 K, there are no detailed studies on their magnetic properties.

In this paper, we examine the structural and magnetic properties of seven members of $A_4B'B_2O_{12}$ by using x-ray diffraction (XRD), AC and DC susceptibility (χ_{AC} , χ_{DC}), neutron powder diffraction (NPD), and specific heat (C_p) measurements. The results reveal that the nature of the magnetic ground state is governed by spin size. For low spin, the compounds are FM with $B' = Ni$ showing FM long range ordering (LRO) and $B' = Co$ showing FM behavior. For high spin ($B' = Mn$), the compound possesses AFM LRO. We propose that this ground state change is due to the competition between two different superexchange interactions present in the structure.

II. EXPERIMENTAL

In total, seven polycrystalline samples of $A_4B'B_2O_{12}$ were prepared by the standard solid state reaction method. They are $Sr_4CoRe_2O_{12}$, $Sr_2La_2CoW_2O_{12}$, $Ba_2La_2CoW_2O_{12}$, $Ba_3LaCoReWO_{12}$, $Ba_4CoRe_2O_{12}$, $Ba_2La_2NiW_2O_{12}$ and $Ba_2La_2MnW_2O_{12}$. Stoichiometric amounts of $BaCO_3/SrCO_3$, La_2O_3 (pre-dried at 980 °C overnight), $CoCO_3/NiO/MnO$, and WO_3/Re metal were mixed in agate mortars, compressed into pellets, and annealed for 20 hours at temperatures of 1000 °C for $Ba_4CoRe_2O_{12}$, 1050 °C for $Ba_3LaCoReWO_{12}$, 1100 °C for $Sr_4CoRe_2O_{12}$, and 1250 °C for $Ba_2La_2CoW_2O_{12}$, $Sr_2La_2CoW_2O_{12}$, $Ba_2La_2MnW_2O_{12}$, and $Ba_2La_2NiW_2O_{12}$.

Powder XRD patterns were performed at room temperature using a HUBER imaging-plate Guinier camera 670 with Ge monochromatized Cu $K\alpha_1$ radiation (1.54059 Å). High-resolution neutron powder diffraction measurements were performed by a neutron powder diffractometer, HB2A, at the High Flux Isotope Reactor (HFIR) of the Oak Ridge National Laboratory (ORNL). Around 3 g of powder was loaded in an Al-cylinder can and mounted in a close-cycled refrigerator. We used a neutron wavelength of $\lambda = 1.5405$ Å with a collimation of 12'-open-6'. Both the XRD and NPD patterns were analyzed by the Rietveld refinement program FullProf³⁶. DC magnetic susceptibility measurements were performed at temperatures of 2-300K using a Quantum Design superconducting interference device (SQUID) magnetometer with an applied field of 0.5 T. AC susceptibility was measured with the conventional mutual inductance technique with a homemade setup³⁷. The specific heat data was obtained using a commercial physical property measurement system (PPMS, Quantum

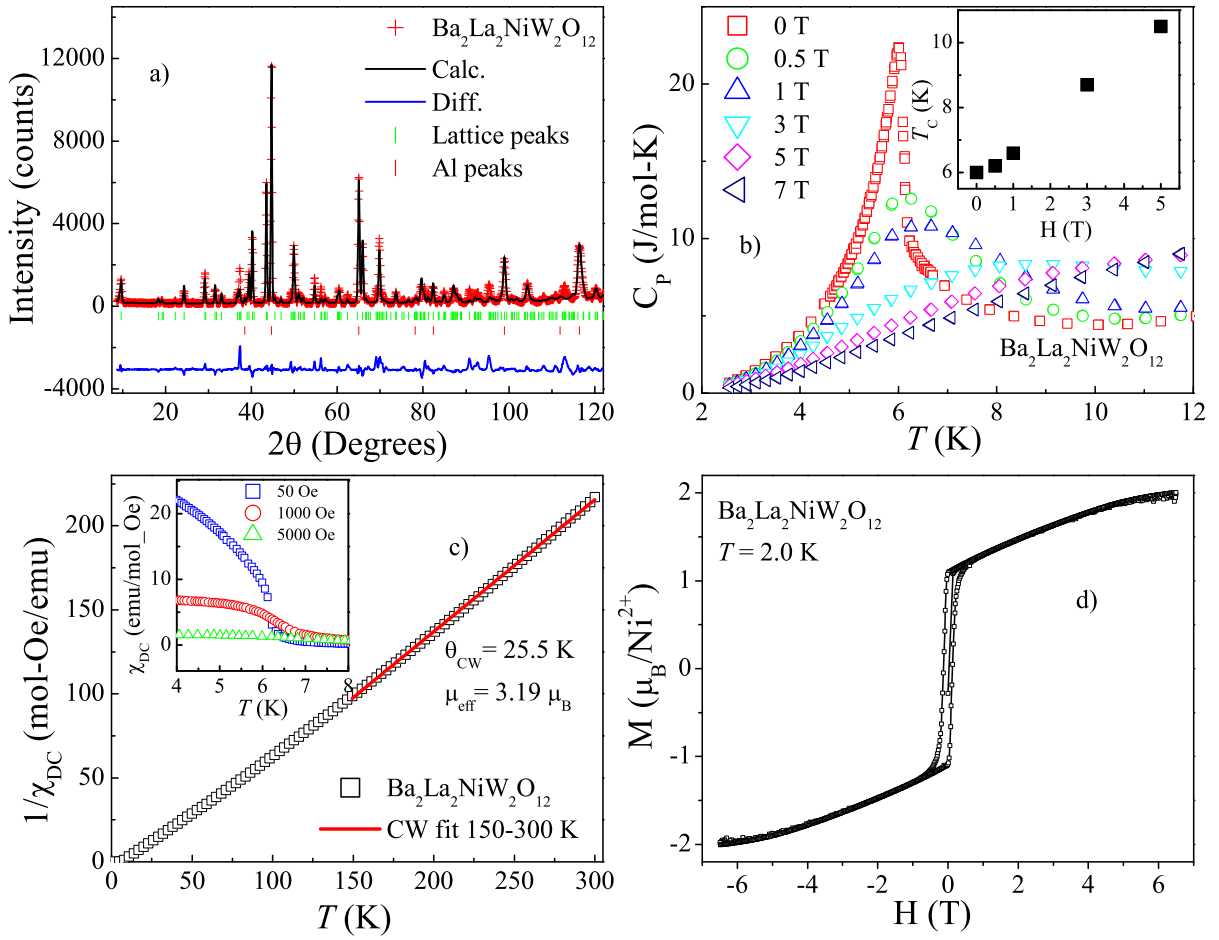


FIG. 5: (color online) For $\text{Ba}_2\text{La}_2\text{NiW}_2\text{O}_{12}$, a) the Rietveld refinement of NPD pattern measured at room temperature using a neutron wavelength of $\lambda = 1.5405 \text{ \AA}$. b) The temperature dependence of the C_p measured at different DC fields. Inset: the field dependence of T_c . c) The inverse DC susceptibility. The solid line is the linear fitting. Inset: the temperature dependence of DC susceptibility measured under different fields. d) The DC magnetization curve measured at 2 K.

Design).

III. RESULTS

Cobalt containing compounds— The refined XRD patterns of five Co containing compounds are shown in Fig. 2. All compounds show pure phases with the space group $R\bar{3}mH$. Used as a continuing example, $\text{Sr}_4\text{CoRe}_2\text{O}_{12}$ has lattice constants of $a = 5.5446(3) \text{ \AA}$ and $c = 26.7382(13) \text{ \AA}$. The refined structural parameters are listed in Table I. It is clear that the lattice parameters are governed by the size of A site ions, with cell volume increasing as strontium is replaced by lanthanum and subsequently replaced by barium. We also tested the refinement by involving the site mixing between Co and W/Re sites. However, the refinements with the extra variable show no improvement from the refinement of the fully ordered structure used here. The results indicate that the site disorder in the compounds is not significant. It could be below 5%, within our XRD resolution.

The inverse DC susceptibility for all five Co containing members is shown in Fig. 3 (a-e). All $1/\chi_{\text{DC}} \sim T$ curves show a slope change around 80 K. Continuing to use $\text{Sr}_4\text{CoRe}_2\text{O}_{12}$ as an example, linear fitting from 150 K to 300 K yields a Curie-Weiss constant of $\theta_{\text{CW}} = -17 \text{ K}$ and $\mu_{\text{eff}} = 4.72 \mu_{\text{B}}$ while the linear fitting from 4.0 K to 15 K yields $\theta_{\text{CW}} = 1.0 \text{ K}$ and $\mu_{\text{eff}} = 3.91 \mu_{\text{B}}$. This change of effective magnetic moment indicates a spin state transition of the Co^{2+} ions from high spin ($S = 3/2$) to low spin ($S = 1/2$). This transition is due to the octahedral environment of the Co^{2+} ions, where the combination of the crystal field and spin orbital coupling lead to a Kramers doublet ground state with effective $S = 1/2$, as described by Low³⁸ and further examined by Lloret et al³⁹. Thus the positive θ_{CW} at low temperatures suggests FM exchange interactions of the effective spin-1/2 Co^{2+} ions. The spin state transition and positive θ_{CW} were also observed for the four other Co compounds by similar linear fittings. The DC magnetization data was taken at 1.8 K, shown in Fig. 3 (a-e) inserts. All data consistently shows a tendency of saturation around $\mu_0 H_s \approx 3 \text{ T}$. To account for Van Vleck paramagnetism,

TABLE I: Structural parameters for the Co containing compounds at room temperature (space group $R\bar{3}mH$) determined from refined XRD measurements.

Refinement	Atom	Site	x	y	z	Occupancy
$\text{Sr}_4\text{CoRe}_2\text{O}_{12}$ $\chi^2 = 2.29$ (a)	Sr1	6c	0	0	0.12982(5)	0.16666
	Sr2	6c	0	0	0.29351(6)	0.16666
	Co	3a	0	0	0	0.08333
	Re	6c	0	0	0.42186(3)	0.16667
	O1	18h	0.50289(50)	0.49711(50)	0.12312(14)	0.50
	O2	18h	0.49249(53)	0.50751(53)	0.29174(19)	0.50
$a = b = 5.54464(26) \text{ (\AA)}, c = 26.73815(126) \text{ (\AA)}$						
Overall B-factor = 1.332 (\AA^2)						
$\text{Sr}_2\text{La}_2\text{CoW}_2\text{O}_{12}$ $\chi^2 = 5.41$ (b)	Sr	6c	0	0	0.13664(13)	0.16667
	La	6c	0	0	0.28914(8)	0.16667
	Co	3a	0	0	0	0.08333
	W	6c	0	0	0.42105(8)	0.16667
	O1	18h	0.50728(82)	0.49272(82)	0.12425(22)	0.50
	O2	18h	0.48772(73)	0.51228(73)	0.29016(28)	0.50
$a = b = 5.60493(41) \text{ (\AA)}, c = 26.58453(197) \text{ (\AA)}$						
Overall B-factor = 2.211 (\AA^2)						
$\text{Ba}_2\text{La}_2\text{CoW}_2\text{O}_{12}$ $\chi^2 = 3.45$ (c)	Ba	6c	0	0	0.13467(8)	0.16667
	La	6c	0	0	0.29032(7)	0.16667
	Co	3a	0	0	0	0.08333
	W	6c	0	0	0.41635(7)	0.16667
	O1	18h	0.50913(77)	0.49087(77)	0.11994(23)	0.50
	O2	18h	0.48361(62)	0.51639(62)	0.29662(28)	0.50
$a = b = 5.68043(12) \text{ (\AA)}, c = 27.37418(60) \text{ (\AA)}$						
Overall B-factor = 2.671 (\AA^2)						
$\text{Ba}_3\text{LaCoWReO}_{12}$ $\chi^2 = 1.43$ (d)	Ba1	6c	0	0	0.12939(6)	0.12500
	La1	6c	0	0	0.12944(6)	0.04167
	Ba2	6c	0	0	0.29533(6)	0.12500
	La2	6c	0	0	0.29533(6)	0.04167
	Co	3a	0	0	0	0.08333
	W	6c	0	0	0.42185(6)	0.08333
	Re	6c	0	0	0.42185(6)	0.08333
	O1	18h	0.51068(82)	0.48932(82)	0.12143(23)	0.50
	O2	18h	0.48365(80)	0.51635(80)	0.29260(32)	0.50
$a = b = 5.70429(9) \text{ (\AA)}, c = 27.675722(54) \text{ (\AA)}$						
Overall B-factor = 1.757 (\AA^2)						
$\text{Ba}_4\text{CoRe}_2\text{O}_{12}$ $\chi^2 = 4.51$ (e)	Ba1	6c	0	0	0.12911(8)	0.16666
	Ba2	6c	0	0	0.29435(9)	0.16666
	Co	3a	0	0	0	0.08333
	Re	6c	0	0	0.42089(8)	0.16667
	O1	18h	0.50262(108)	0.49738(108)	0.12325(29)	0.50
	O2	18h	0.47513(97)	0.52487(97)	0.28794(41)	0.50
$a = b = 5.72455(33) \text{ (\AA)}, c = 27.76966(161) \text{ (\AA)}$						
Overall B-factor = 1.694 (\AA^2)						

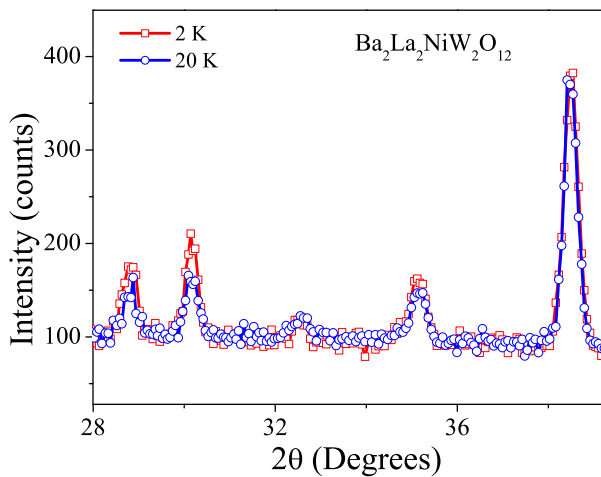


FIG. 6: (color online) NPD of $\text{Ba}_2\text{La}_2\text{NiW}_2\text{O}_{12}$ taken at 2 K and 20 K. The overlap of magnetic Bragg peaks with lattice Bragg peaks indicates FM long range ordering.

a linear fit of high field data was used to calculate the saturation magnetization (M_S). For $\text{Sr}_4\text{CoRe}_2\text{O}_{12}$, the extrapolation yields a value of $M_S = 1.52 \mu_B/\text{Co}^{2+}$ and a powder-averaged gyromagnetic ratio $g = 3.04$. For the four other compounds, the obtained g is around $3 \sim 4.2$. All of the magnetic parameters are summarized in Table III.

The real part of the AC susceptibility measurements taken under different DC fields for the Co compounds are shown in Fig. 4. Continuing use of $\text{Sr}_4\text{CoRe}_2\text{O}_{12}$ as an example, its χ_{AC} shows a fast increase with decreasing temperature below 1.5 K followed by a broad peak. This feature, while not strong enough evidence to claim LRO, is evidence for FM behavior such as the formation of FM clusters or FM correlations. Here we define the FM behavior temperatures (T_{FM}) as the local minima position in the first derivative of χ_{AC} , which is 1.0 K for $\text{Sr}_4\text{CoRe}_2\text{O}_{12}$. With increasing DC field, this broad peak shifts to higher temperatures while simultaneously decreasing in magnitude. This increase of T_{FM} under applied field further indicates a FM nature which is consistent with the DC susceptibility results. The four other Co compounds show similar χ_{AC} behavior with different T_{FM} , which are listed in Table III. Therefore, all five Co compounds show FM behavior around 1 K. One noteworthy feature is that for $\text{Sr}_2\text{La}_2\text{CoW}_2\text{O}_{12}$ and $\text{Ba}_2\text{La}_2\text{CoW}_2\text{O}_{12}$, the χ_{AC} shows a second peak at lower temperatures below 1 K when a 0.05 T DC field was applied. Whether this feature represents further FM behavior requires further exploration.

$\text{Ba}_2\text{La}_2\text{NiW}_2\text{O}_{12}$ – The Rietveld refinement performed on the NPD pattern (Fig. 5(a)) measured at room temperature confirms the pure phase with space group $R\bar{3}mH$ for $\text{Ba}_2\text{La}_2\text{NiW}_2\text{O}_{12}$. The refined structural parameters are $a = 5.6622(4) \text{ \AA}$ and $c = 27.3661(22) \text{ \AA}$. The detailed structural parameters are listed in Table II. Under zero field, the specific heat data (Fig. 5(b)) shows a sharp peak at 6.2 K in agreement with T_C from χ_{DC} . Under applied DC fields, this peak broadens out and occurs at higher temperatures. The transition

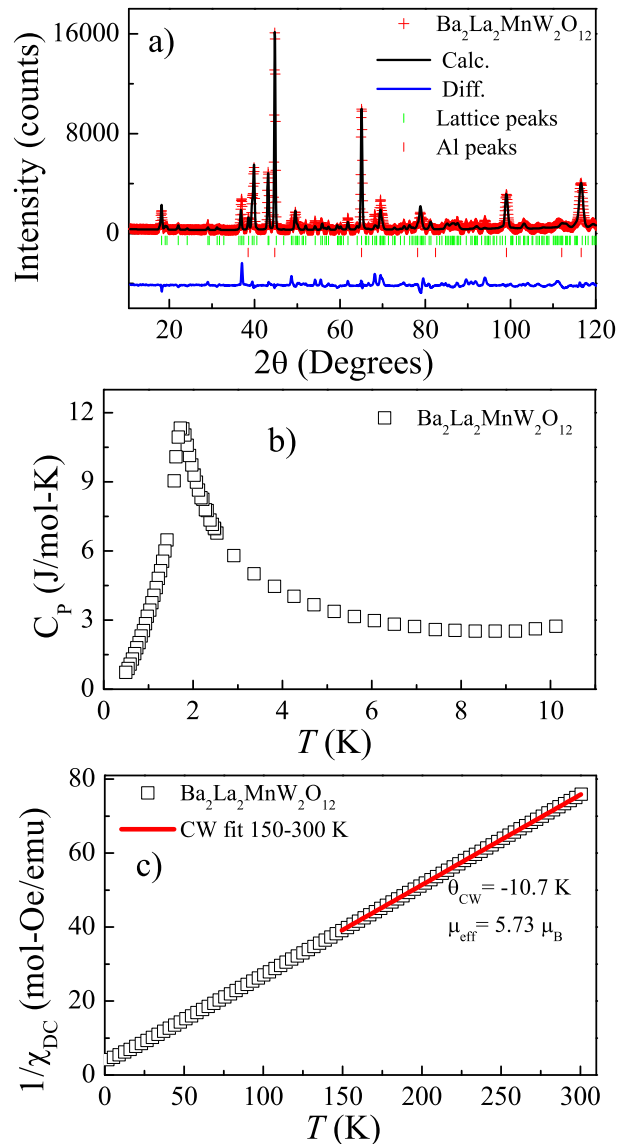


FIG. 7: (color online) For $\text{Ba}_2\text{La}_2\text{MnW}_2\text{O}_{12}$, a) the Rietveld refinement of the NPD pattern taken at room temperature. b) The temperature dependence of the C_P measured at zero field. c) The inverse DC susceptibility. The solid line is the linear fitting.

temperature (the peak position) increases linearly with the increasing field as shown in the insert of Fig. 5(b). The linear fitting of the inverse DC susceptibility from 150 to 300 K (Fig. 5(c)) yields a positive $\theta_{CW} = 25.5 \text{ K}$ and $\mu_{eff} = 3.19 \mu_B$, indicating FM interactions. As shown in the insert of Fig. 5(c), the χ_{DC} measured at 50 Oe clearly shows a sharp transition at $T_C = 6.2 \text{ K}$ (defined as the minimum in $d\chi_{DC}/dT$). With increasing field, this transition becomes broader and shifts to higher temperatures, which again verifies its FM nature. The DC magnetization data taken at 2.0 K (Fig. 5(d)) clearly shows a hysteresis loop and a saturation value at $M_S \approx 2 \mu_B$. NPD performed at 2 K and 20 K shows clear magnetic Bragg peaks overlapping lattice Bragg peaks (Fig. 6), confirming the on-

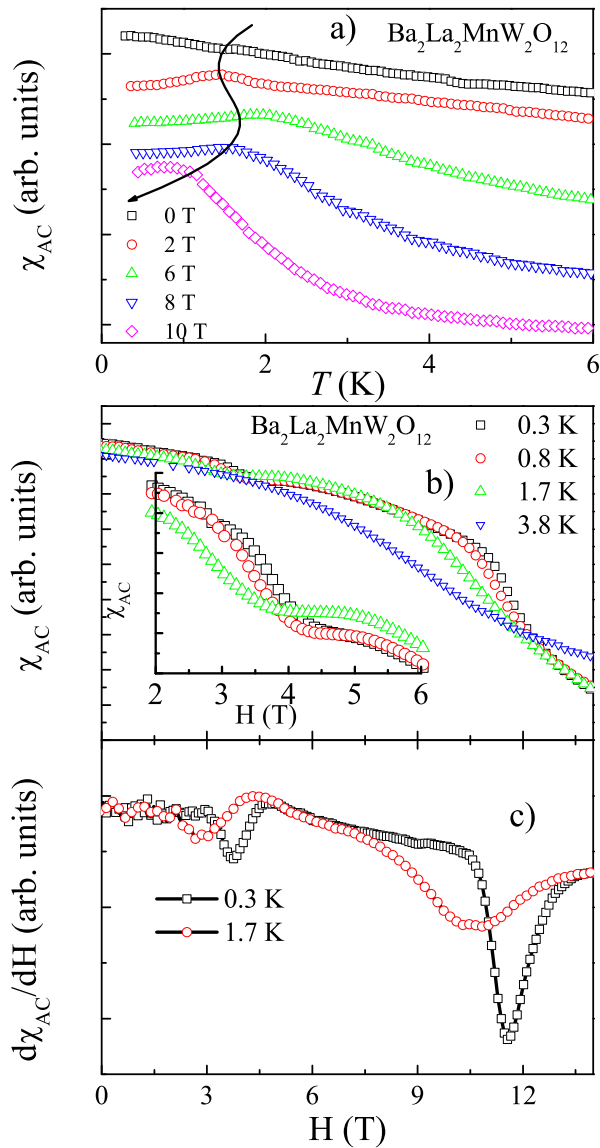


FIG. 8: (color online) a) The temperature dependence of χ_{AC} for $Ba_2La_2MnW_2O_{12}$ under applied DC fields. b) The DC Field dependence of χ_{AC} at various temperatures. Insert: the enlargement of the data around 4 T. c) The derivative of the field dependence of χ_{AC} at different temperatures.

set of FM LRO. Refinement of the ferromagnetic contribution results in a magnetic moment $\approx 2 \mu_B$, consistent with the magnetization data. Due to the powder nature of the sample, the spin orientation cannot be resolved. All of this data, such as the peak of C_p and fast increase of χ_{DC} at 6.2 K, the positive θ_{CW} , the hysteresis loop of magnetization, the increase of T_C under fields, and magnetic Bragg peaks from NPD consistently show that $Ba_2La_2NiW_2O_{12}$ is a spin-1 system with long range FM ordering at 6.2 K.

$Ba_2La_2MnW_2O_{12}$ —The Rietveld refinement performed on the NPD pattern measured at room temperature (Fig. 7(a)) confirms the pure phase with space group $R\bar{3}mH$ for

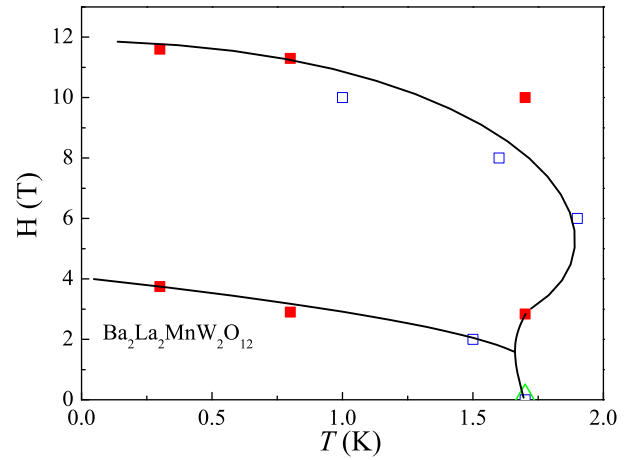


FIG. 9: (color online) Magnetic phase diagram of $Ba_2La_2MnW_2O_{12}$. Transition temperatures were found from the temperature derivative (red solid squares), the field derivative (blue open squares) of χ_{AC} , and zero field C_p measurements (green triangle).

$Ba_2La_2MnW_2O_{12}$. The refined structural parameters are $a = 5.7280(4) \text{ \AA}$ and $c = 27.3872(38) \text{ \AA}$. The detailed structural parameters are listed in Table II. The specific heat data (Fig. 7(b)) shows a sharp peak at $T_N = 1.7 \text{ K}$, which should represent AFM long range ordering. The linear fitting of the inverse DC susceptibility from 150 to 300 K (Fig. 7(c)) yields a negative $\theta_{CW} = -10.7 \text{ K}$ and $\mu_{eff} = 5.73 \mu_B$, indicating AFM interactions.

The χ_{AC} was measured as a function of temperature under varying applied DC fields (Fig. 8(a)) and as a function of DC field under applied temperatures (Fig. 8(b)). Here, transitions were again found using local minima of $d\chi_{AC}/dT$ and $d\chi_{AC}/dH$. As shown in Fig. 8(a), at zero field, the temperature dependence of χ_{AC} shows no significant feature but a weak slope change around 1.7 K, which is consistent with the T_N observed from the specific heat. Then, with $H = 2 \text{ T}$, there is a peak that appears at 1.5 K. Thereafter, this peak position shifts to higher temperatures first and then shifts to lower temperatures with increasing DC field, as indicated by the curved arrow in Fig. 8(a). Meanwhile, the field scan performed at 0.3 K shows two slope changes around 4 T and 11 T. These two features are more clearly visible as the two sharp valleys from the $d\chi_{AC}/dH$ curve (Fig. 8(c)). Here we define the minima positions as $H_{c1} = 3.75 \text{ T}$ and $H_{c2} = 11.6 \text{ T}$. With increasing temperature, these two features become broader and shift to lower fields. Above T_N , they disappear. A magnetic phase diagram of $Ba_2La_2MnW_2O_{12}$ was constructed by the transition temperatures and critical field values obtained from C_p and χ_{AC} , as shown in Fig. 9.

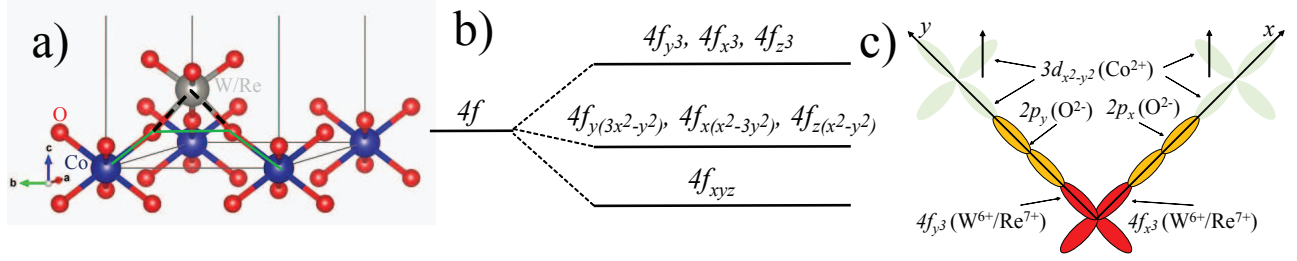


FIG. 10: (color online) a) Pathways for FM B'-O-B'-O-B' (black dashed) and AFM B'-O-O-B' (green solid) superexchange interactions. b) Energy levels of $4f$ orbitals in cubic symmetry, with highest energy levels having the same symmetry as p -orbitals. c) Orbital diagram of FM B'-O-B'-O-B' interaction with f orbitals represented by symmetrically similar p orbitals.

TABLE II: Structural parameters for $\text{Ba}_2\text{La}_2\text{NiW}_2\text{O}_{12}$ and $\text{Ba}_2\text{La}_2\text{MnW}_2\text{O}_{12}$ at room temperature (space group $R\bar{3}mH$) determined from refined NPD measurements.

Refinement	Atom	Site	x	y	z	Occupancy
$\text{Ba}_2\text{La}_2\text{NiW}_2\text{O}_{12}$ (a)	Ba	6c	0	0	0.13324(60)	0.16667
	La	6c	0	0	0.29309(44)	0.16667
	Ni	3a	0	0	0	0.08333
	W	6c	0	0	0.41881(68)	0.16667
	O1	18h	0.49760(81)	0.50240(81)	0.11707(27)	0.50
	O2	18h	0.47868(74)	0.52132(74)	0.29302(37)	0.50
$a = b = 5.66221(40)$ (Å), $c = 27.36606(224)$ (Å)						
Overall B-factor = 1.401 (Å ²)						
Refinement	Atom	Site	x	y	z	Occupancy
$\text{Ba}_2\text{La}_2\text{MnW}_2\text{O}_{12}$ (b)	Ba	6c	0	0	0.13551(85)	0.16667
	La	6c	0	0	0.29341(47)	0.16667
	Mn	3a	0	0	0	0.08333
	W	6c	0	0	0.41653(86)	0.16667
	O1	18h	0.49847(95)	0.50153 (95)	0.11839(30)	0.50
	O2	18h	0.47415(88)	0.52586(88)	0.29343(38)	0.50
$a = b = 5.72804(74)$ (Å), $c = 27.38715(384)$ (Å)						
Overall B-factor = 1.558 (Å ²)						

IV. DISCUSSION

It is obvious that the spin number of the magnetic B' ions significantly affects the magnetic ground states of the studied $\text{A}_4\text{B}'\text{B}_2\text{O}_{12}$ compounds, which manifest FM ordering for the Co^{2+} ($S = 1/2$) and Ni^{2+} ($S = 1$) compounds but AFM ordering for the Mn^{2+} ($S = 5/2$) compound. To understand this drastic ground state change, we examine the superexchange interactions of the B'^{2+} ions in the structure. Using the theoretical framework laid down by Kanamori⁴⁰, a qualitative description of the superexchange interaction between magnetic cations on an octahedral site can be determined from the orbital configurations of the magnetic cations and the nonmagnetic, bridging anions. In $\text{A}_4\text{B}'\text{B}_2\text{O}_{12}$, octahedra of $\text{B}'\text{O}_6$ are corner sharing with octahedra of BO_6 via an oxygen, providing two pathways for intralayer superexchange. These paths are $\text{B}'^{2+}\text{-O}^{2-}\text{-O}^{2-}\text{-B}'^{2+}$ with the other being $\text{B}'^{2+}\text{-O}^{2-}\text{-W}^{6+}\text{-O}^{2-}\text{-B}'^{2+}$ or $\text{B}'^{2+}\text{-O}^{2-}\text{-Re}^{7+}\text{-O}^{2-}$

B'^{2+} , as show in Fig. 10(a). The superexchange pathway along $\text{B}'^{2+}\text{-O}^{2-}\text{-O}^{2-}\text{-B}'^{2+}$ is commonly found in other magnetic oxides, where the interaction is AFM.

Meanwhile, for W^{6+} and Re^{7+} ions on octahedral sites, the cubic crystal field splits their degenerate $4f$ orbitals (the filled outermost orbitals) into three groups as shown in Fig. 10(b). The group of f_{x^3} , f_{y^3} , and f_{z^3} with t_{1g} symmetry mainly participate in the orbital hybridization with the $\text{O}^{2-}\text{-}2p$ orbitals due to geometrical reasons. Thus, one possible situation for the $\text{B}'^{2+}\text{-O}^{2-}\text{-W}^{6+}\text{-O}^{2-}\text{-Cr}^{3+}$ exchange path, which is similar for the Re case, is shown in Fig. 10(c). Here we consider the superexchange interaction between the spins on the $d_{x^2-y^2}$ orbitals of the B'^{2+} ions and assume that the B'^{2+} , O^{2-} and W^{6+} ions are on the same line and that the $\text{O}^{2-}\text{-W}^{6+}\text{-O}^{2-}$ bond angle is 90° . In this situation, spin 1 on the left B'^{2+} ion is transferred to the molecular orbital composed of the p_y orbitals of the O^{2-} $2p$ orbitals and the f_{y^3} orbitals of the W^{6+} $4f$ orbitals; meanwhile, spin 2 on the right B'^{2+}

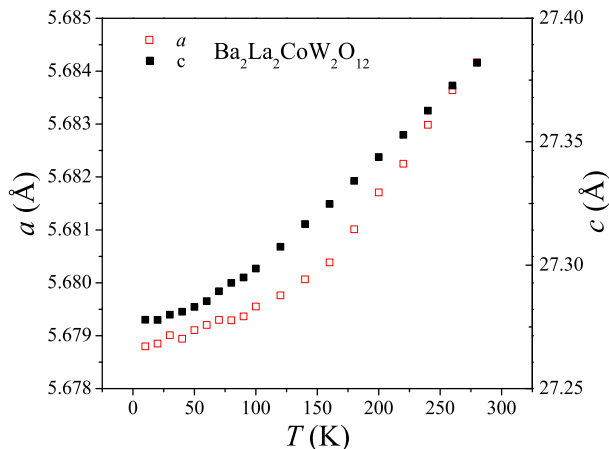


FIG. 11: (color online) Temperature dependence of lattice parameters a and c for $\text{Ba}_2\text{La}_2\text{CoW}_2\text{O}_{12}$. No structural distortion is seen upon the transition from high spin ($S = 3/2$) to low spin ($S = 1/2$) of the Co^{2+} ions.

ion is transferred to the molecular orbital composed of the p_x orbitals of O^{2-} and the f_{x^3} orbitals of W^{6+} ions. Due to Hund's rules, these two spins on the f_{y^3} and f_{x^3} orbitals in the W^{6+} ions have to be parallel. Then, after these two spins are transferred back to the B'^{2+} ion, a FM superexchange interaction between them is formed. With these two different superexchanges in the system, it is natural to propose that the ground state change is due to the competition between them. This means the FM interaction exceeds the AFM interaction for spin-1/2 and 1 systems, but AFM interactions are stronger for the spin-5/2 system.

Since the t_{1g} symmetry of the $4f$ orbitals here is identical to the symmetry of the p orbitals of $4p$ or $3p$ orbitals, similar FM superexchange interactions should also occur for $3d-2p-4p$ (or $3p$)- $2p-3d$ paths. Several other TLMS with layered perovskite structures have been observed to possess such FM superexchange interactions. Similar competitive FM and AFM superexchanges are observed in $\text{Ba}_3\text{CoNb}_2\text{O}_9$ ¹³, where the $\text{Co}^{2+}-\text{O}^{2-}-\text{Nb}^{5+}-\text{O}^{2-}-\text{Co}^{2+}$ superexchange interaction involving the Nb^{5+} $4p$ orbitals is FM, and it opposes the AFM $\text{Co}^{2+}-\text{O}^{2-}-\text{O}^{2-}-\text{Co}^{2+}$ interaction leading to a weaker AFM interaction. This manifests in a low AFM transition temperature as well as a low saturation field. Alternatively, $\text{A}\text{Ag}_2\text{M}(\text{VO}_4)_2$ ($\text{A}=\text{Ba}, \text{Sr}; \text{M}=\text{Co}, \text{Ni}$)²² has a stronger FM superexchange via $\text{Co}^{2+}-\text{O}^{2-}-\text{V}^{5+}-\text{O}^{2-}-\text{Co}^{2+}$ than AFM superexchange via $\text{Co}^{2+}-\text{O}^{2-}-\text{O}^{2-}-\text{Co}^{2+}$ and possesses an FM transition.

Next, we look into the chemical pressure effect among the Co samples. In general, the increasing lattice parameter should decrease the exchange interactions and therefore lead to a lowered T_{FM} . However, this is not the case here. Instead, with increasing lattice parameter, the T_{FM} first increases from Sr_4 to Sr_2La_2 and then to the Ba_2La_2 sample, afterwards it decreases to Ba_3La and to the Ba_4 sample. To explore the more general rule behind this chemical pressure effect, we

must turn to more detailed structural information. Fig. 11 shows that there is no structural distortion upon cooling from the high spin ($S = 3/2$) to low spin ($S = 1/2$) states of the Co^{2+} ion. Thus the substitution of A site ions will provide isostructural chemical pressure, as seen in the XRD refinements, even at low temperatures. Unfortunately, the angle of the O-B-O bond cannot be resolved sufficiently with the available XRD resolution. Further neutron studies will be pursued to examine if there is further evidence to explain the fine tuning of the Co sample FM behavior temperature.

Finally, we comment on the phase diagram of $\text{Ba}_2\text{La}_2\text{MnW}_2\text{O}_{12}$. One common ground state at zero field observed for studied triangular lattice antiferromagnets (TLAFs), such as $\text{Ba}_3\text{CoSb}_2\text{O}_9$ ⁷ and $\text{Ba}_3\text{BNb}_2\text{O}_9$ ($\text{B} = \text{Co}^{12,13}, \text{Ni}^{14}, \text{Mn}^{15}$), is the 120 degree ordered state. The phase diagrams of these TLAFs consistently show a canted 120 degree, up up down, oblique, and polarized phases with increasing applied magnetic field. Comparing the phase diagram of $\text{Ba}_2\text{La}_2\text{MnW}_2\text{O}_{12}$ to theirs, the overall trend is similar. Therefore, we tend to ascribe its zero field ground state to be 120 degree ordering. With increasing field it enters the canted 120 degree phase below H_{c1} , up up down phase above H_{c1} , and then polarized phase above H_{c2} . One difference here is that we do not observe the oblique phase boundary between the up up down and polarized phases for $\text{Ba}_2\text{La}_2\text{MnW}_2\text{O}_{12}$. One possibility is that our AC measurements do not have the resolution to detect this phase boundary due to the polycrystalline nature of the sample.

V. CONCLUSION

We have examined the structural and magnetic properties of a family of $\text{A}_4\text{B}'\text{B}_2\text{O}_{12}$ compounds with a 2D magnetic triangular lattice. Due to the competition between two kinds of superexchange interactions (one FM and one AFM) in the structure, the ground states of the triangular lattice can be efficiently tuned by varying the spin numbers of the magnetic B'^{2+} ions. The result is FM behavior or ordering for the Co and Ni samples, respectively, with small spin numbers and AFM ordering for the Mn samples with a large spin number. Moreover, the chemical pressure can finely tune the FM behavior temperature and effective exchange interactions among the Co sample via a mechanism remaining to be explored. These findings demonstrate that $\text{A}_4\text{B}'\text{B}_2\text{O}_{12}$ is a new platform for TLMs waiting for future exploration to study geometrically frustrated magnetism.

Acknowledgments

R.R. and H.D.Z. thank the support from NSF-DMR through Award DMR-1350002. J.M. thanks the support of the Ministry of Science and Technology of China (2016YFA0300500). The research at HFIR/ORNL was sponsored by the Scientific User Facilities Division, Office of Basic Energy Sciences, US Department of Energy. The work at

TABLE III: Summary of magnetic properties (FM behavior, FM transition, and AFM transition temperatures T_{FM} , T_C , T_N , Curie-Weiss constant θ_{CW} , effective magnetic moment μ_{eff} , saturation magnetization M_S , and gyromagnetic ratio g) of $A_4B'B_2O_{12}$ compounds

Compound	$T_{\text{FM}}/T_C/T_N$ (K)	θ_{CW} (K)	μ_{eff} (μ_B)	M_S (μ_B)	g
$\text{Sr}_4\text{CoRe}_2\text{O}_{12}$	1.0	1.0	3.91	1.5	3.0
$\text{Sr}_2\text{La}_2\text{CoW}_2\text{O}_{12}$	1.26	1.5	3.95	2.0	4.0
$\text{Ba}_2\text{La}_2\text{CoW}_2\text{O}_{12}$	1.28	1.6	4.01	2.1	4.2
$\text{Ba}_3\text{LaCoReWO}_{12}$	0.83	0.78	3.89	1.9	3.8
$\text{Ba}_4\text{CoRe}_2\text{O}_{12}$	0.87	0.61	3.87	1.6	3.2
$\text{Ba}_2\text{La}_2\text{NiW}_2\text{O}_{12}$	6.2	25.5	3.19	≈ 2	≈ 2
$\text{Ba}_2\text{La}_2\text{MnW}_2\text{O}_{12}$	1.7	-10.7	5.73	–	–

NHMFL is supported by NSF-DMR-1157490 and the State of Florida.

- ¹ A. P. Ramirez, *Annu. Rev. Mater. Sci.* **24**, 453 (1994).
- ² L. Balents, *Nature* **464**, 199 (2010).
- ³ J. Greedan, *J. Mater. Chem.* **11**, 37 (2000).
- ⁴ M. F. Collins and O. A. Petrenko, *Can. J. Phys.* **75**, 605 (1997).
- ⁵ A. V. Chubukov and D. I. Golosov, *J. Phys.:Condens. Matter* **3**, 69 (1991).
- ⁶ O. A. Starykh, W. Jin, and A. V. Chubukov, *Phys. Rev. Lett.* **113**, 087204 (2014).
- ⁷ H. D. Zhou, C. Xu, A. M. Hallas, H. J. Silverstein, C. R. Wiebe, I. Umegaki, J. Q. Yan, T. P. Murphy, J. -H. Park, Y. Qiu, J. R. D. Copley, J. S. Gardner, and Y. Takano, *Phys. Rev. Lett.* **109**, 267206 (2012).
- ⁸ T. Susuki, N. Kurita, T. Tanaka, H. Nojiri, A. Matsuo, K. Kindo, and H. Tanaka, *Phys. Rev. Lett.* **110**, 267201 (2013).
- ⁹ G. Quirion, M. Lapointe-Major, M. Poirier, J. A. Quilliam, Z. L. Dun, and H. D. Zhou, *Phys. Rev. B* **92**, 014414 (2015).
- ¹⁰ G. Koutroulakis, T. Zhou, Y. Kamiya, J. D. Thompson, H. D. Zhou, C. D. Batista, and S. E. Brown, *Phys. Rev. B* **91**, 024410 (2015).
- ¹¹ J. Ma, Y. Kamiya, T. Hong, H. B. Cao, G. Ehlers, W. Tian, C. D. Batista, Z. L. Dun, H. D. Zhou, and M. Matsuda, *Phys. Rev. Lett.* **116**, 087201 (2016).
- ¹² M. Lee, J. Hwang, E. S. Choi, J. Ma, C. R. Dela Cruz, M. Zhu, X. Ke, Z. L. Dun, and H. D. Zhou, *Phys. Rev. B* **89**, 104420 (2014).
- ¹³ K. Yokota, N. Kurita, and H. Tanaka, *Phys. Rev. B* **90**, 014403 (2014).
- ¹⁴ J. Hwang, E. S. Choi, F. Ye, C. R. Dela Cruz, Y. Xin, H. D. Zhou, and P. Schlottmann, *Phys. Rev. Lett.* **109**, 257205 (2012).
- ¹⁵ M. Lee, E. S. Choi, X. Huang, J. Ma, C. R. Dela Cruz, M. Matsuda, W. Tian, Z. L. Dun, S. Dong, and H. D. Zhou, *Phys. Rev. B* **90**, 224402 (2014).
- ¹⁶ H. Kadowaki, H. Kikuchi, and Y. Ajiro, *J. Phys.: Condens. Matter* **2**, 4485 (1990).
- ¹⁷ K. Kimura, H. Nakamura, K. Ohgushi, and T. Kimura, *Phys. Rev. B* **78**, 140401 (2008).
- ¹⁸ M. Kenzelmann, G. Lawes, A. B. Harris, G. Gasparovic, C. Broholm, A. P. Ramirez, G. A. Jorge, M. Jaime, S. Park, Q. Huang, A. Ya. Shapiro, and L. A. Demianets, *Phys. Rev. Lett.* **98**, 267205 (2007).
- ¹⁹ A. B. Harris, *Phys. Rev. B* **76**, 054447 (2007).
- ²⁰ E. Wawrzyńska, R. Coldea, E. M. Wheeler, I. I. Mazin, M. D. Johannes, T. Sörgel, M. Jansen, R. M. Ibberson, and P. G. Radaelli, *Phys. Rev. Lett.* **99**, 157204 (2007).
- ²¹ E. M. Wheeler, R. Coldea, E. Wawrzyńska, T. Sörgel, M. Jansen, M. M. Koza, J. Taylor, P. Adroguer, and N. Shannon, *Phys. Rev. B* **79**, 104421 (2009).
- ²² A. Möller, N. E. Amunke, P. Daniel, B. Lorenz, C. R. dela Cruz, M. Gooch, and P. C. W. Chu, *Phys. Rev. B* **85**, 214422 (2012).
- ²³ A. A. Tsirlin, A. Möller, B. Lorenz, Y. Skourski, and H. Rosner, *Phys. Rev. B* **85**, 014401 (2012).
- ²⁴ T. M. McQueen, P. W. Stephens, Q. Huang, T. Klimczuk, F. Ronning, and R. J. Cava, *Phys. Rev. Lett.* **101**, 166402 (2008).
- ²⁵ T. Jia, G. R. Zhang, Z. Zeng, and H. Q. Lin, *Phys. Rev. B* **80**, 045103 (2009).
- ²⁶ Y. Li, G. Chen, W. Tong, L. Pi, J. Liu, Z. Yang, X. Wang, and Q. Zhang, *Phys. Rev. Lett.* **115**, 167203 (2015).
- ²⁷ Y. Li, H. Liao, Z. Zhang, S. Li, F. Jin, L. Ling, L. Zhang, Y. Zou, L. Pi, Z. Yang, J. Wang, Z. Wu, and Q. Zhang, *Scientific Reports* **5**, 16419 (2015).
- ²⁸ Y. Shen, Y. D. Li, H. Wo, Y. Li, S. Shen, B. Pan, Q. Wang, H. C. Walker, P. Steffens, M. Boehm, Y. Hao, D. L. Quintero-Castro, L. W. Harriger, M. D. Frontzek, L. Hao, S. Meng, Q. Zhang, G. Chen, and J. Zhao, *Nature* **540**, 559 (2016).
- ²⁹ J. A. M. Paddison, M. Daum, Z. Dun, G. Ehlers, Y. Liu, M. B. Stone, H. D. Zhou, and M. Mourigal, *Nature Physics* **13**, 117 (2016).
- ³⁰ L. Katz and R. Ward, *Inorg. Chem.* **3**, 205 (1964).
- ³¹ A. Maignan, W. Kobayashi, S. Hébert, G. Martinet, D. Pelloquin, N. Bellido, and Ch. Simon, *Inorg. Chem.* **47**, 8553 (2008).
- ³² J. M. Longo, L. Katz, and R. Ward, *Inorg. Chem.* **4**, 235 (1965).
- ³³ H. J. Rother, A. Fadini, and S. Kemmler-Sack, *Z. Anorg. Allg. Chem.* **463**, 137 (1980).
- ³⁴ S. Kemmler-Sack, *Z. Anorg. Allg. Chem.* **461**, 142 (1980).
- ³⁵ Z. F. Li, J. L. Sun, L. P. You, Y. X. Wang, and J. H. Lin, *J. Alloy. Compd.* **379**, 117 (2004).
- ³⁶ J. Rodriguez-Carvajal, *Physica B* **192**, 55 (1993).
- ³⁷ Z. L. Dun, M. Lee, E. S. Choi, A. M. Hallas, C. R. Wiebe, J. S. Gardner, E. Arrighi, R. S. Freitas, A. M. Arevalo-Lopez, J. P. Attfield, H. D. Zhou, and J. G. Cheng, *Phys. Rev. B* **89**, 064401 (2014).
- ³⁸ W. Low, *Phys. Rev.* **109**, 256 (1958).
- ³⁹ F. Lloret, M. Julve, J. Cano, R. Ruiz-García, and E. Pardo, *Inorg. Chim. Acta.* **361**, 3432 (2008).
- ⁴⁰ J. Kanamori, *J. Phys. Chem. Solids* **10**, 87 (1959).